

Heavy Element Abundances in Binary Neutron Star Mergers

NICOLE MULYK

ABSTRACT

Binary neutron star mergers have recently been seriously considered a viable source of rapid neutron capture process (r-process) elements. The r-process is one of the primary methods for producing heavy elements and requires a very neutron-rich environment. In this paper, I discuss how the parameters of hypermassive neutron stars affects the amount of r-process elements produced in the ejecta of the disk. First, I post-processed the hydrodynamic trajectories from [Fahlman & Fernández \(2018\)](#) using SkyNet to simulate nuclear reactions in the torus’ ejecta. Then, I explored the process behind the variation in mass fraction of heavy elements, paying close attention to what processes alter the electron fraction. There are many subtleties explored in Section 4; however in general, a model with a low viscosity parameter, low initial neutrino luminosity, low central HMNS mass, or a high initial torus mass will have an increased level of heavy elements being produced.

1. INTRODUCTION

The gravitational wave detection, GW170817, was first observed in August 2017 by Advanced LIGO/Virgo ([Curtis et al. 2021](#); [Metzger 2019](#)). The gravitational waves were caused by the merger of two neutron stars, which spiraled inward towards each other as their orbits decayed. The result of a binary neutron star merger (NS-NS merger) is a hypermassive neutron star (HMNS) that may collapse into a black hole following a short HMNS lifetime. The detection of GW170817 launched the field of multi-messenger astronomy, introduced gravitational waves as a tool for studying astronomy, and was also an excellent opportunity to verify theoretical predictions ([Siegel \(2019\)](#); [Metzger \(2019\)](#)).

GW170817 provided an exceptional opportunity to verify the theoretical prediction that NS-NS mergers produce and are possibly the dominant source of rapid neutron capture process (r-process) elements ([Kasen et al. 2017](#)). Sixty years prior to the detection of GW170817, [Cameron \(1957\)](#) and [Burbidge et al. \(1957\)](#) independently suggested that heavy elements could be produced by neutron capture in a neutron-rich environment ([Metzger 2019](#)). The r-process could be responsible for producing more than half of the elements heavier than iron, yet its origin is still largely unknown. The r-process occurs when a nucleus in a neutron-rich environment will capture a neutron from its surroundings, creating a heavier, unstable nucleus. This nucleus then decays back to a stable state, producing a kilonova that scientists on Earth can detect.

Following the detection of GW170817, several follow-up measurements were made so that the entire electromagnetic spectrum could be used to observe the transient counterpart ([Siegel 2019](#)). The results agreed with the theoretical prediction of a kilonova powered by the decay of r-process elements. The initial optical emis-

sion during the first day following the merger suggests that the kilonova was powered by the radioactive decay of light r-process elements (with mass numbers $A \leq 140$) ([Metzger 2019](#)). In the following days, a near-infrared emission was sighted, predicting the presence of heavy r-process elements ($A \geq 140$) in the inner layers of the ejecta. The large amount of r-process elements produced and the high merger rate are highly suggestive that NS-NS mergers are a significant source of r-process elements.

The electron fraction, Y_e , is an important indicator since a neutron-rich environment is required for the r-process to occur. Y_e can be calculated with Equation 1 ([Curtis et al. 2021](#)).

$$Y_e = \frac{n_p}{n_p + n_n} \quad (1)$$

where n_p is the number density of protons, n_n is the number density of neutrons, and $n_p + n_n$ is the number density of total baryons. Technically, Equation 1 is calculating the proton fraction, but this is equivalent to the electron fraction due to charge conservation. For the r-process to occur, $Y_e \lesssim 0.25$ is required to produce elements with $A \geq 130$ ([Metzger 2019](#)). For this project, I focused on what processes alter Y_e in an NS-NS merger model.

[Fahlman & Fernández \(2018\)](#) simulated HMNS disk outflows using FLASH3, a hydrodynamic simulation code, to create several models whose parameters were consistent with the observations of GW170817. The torus formed around an HMNS recently produced by an NS-NS merger. The simulations began after the formation of an HMNS but before the collapse to a black hole. I post-processed the hydrodynamic results from [Fahlman & Fernández \(2018\)](#) with SkyNet, a nuclear reaction network code that simulates nucleosynthesis in

Table 1. Models and their parameters. The columns from left to right are model name, viscosity parameter, initial HMNS neutrino luminosity, central object mass, and initial torus mass.

Model	α	$L_{ve}(erg\ s^{-1})$	$M_{NS}(M_{\odot})$	$M_t(M_{\odot})$
base	0.05	2×10^{52}	2.65	0.10
$\alpha 0.03$	0.03
$\alpha 0.10$	0.10
L51	0.05	2×10^{51}
L53	...	2×10^{53}
m2.6	...	2×10^{52}	2.60	...
m2.7	2.70	...
mt02	2.65	0.20
mt03	0.30

the disk outflow. I obtained the resulting abundances of each element produced during the simulation. Initially, I explored the effects of electron neutrinos, one of the main processes that can alter Y_e . However, this was extensively covered in the midterm report. So, I will instead focus on how the parameters of each model can affect Y_e . Since each model had an initial electron fraction of 0.10, altering parameters, such as the viscosity parameter, initial HMNS neutrino luminosity, central object mass, and initial torus mass, can have varying effects on Y_e .

In Section 2, the simulation codes, models, and relevant equations will be discussed. Section 3 outlines the results of this project, and Section 4 explains what those results mean in the context of how the altered parameters change the amount of r-process elements being produced.

2. METHODS

Fahlman & Fernández (2018) created multiple models, each varying one parameter from the base model. I have focused on nine models for this project, including the base model. The eight remaining models have one of the following parameters adjusted from the value in the base model: viscosity parameter α , initial HMNS neutrino luminosity L_{ve} , central object mass M_{NS} , and initial torus mass M_t . The model’s name and its parameters are presented in Table 1.

The following conditions were set for all models discussed in this project: HMNS radius = 20 km, torus radius = 50 km, initial $Y_e = 0.10$, HMNS lifetime = 10 ms, and initial torus entropy = $8\ k_B/\text{baryon}$. Each model contains several trajectories consisting of the properties of a single tracer particle. I post-processed these trajec-

tories in SkyNet, which simulated nucleosynthesis in the hypermassive neutron star disk outflow, and then performed analysis on the trajectories and SkyNet results.

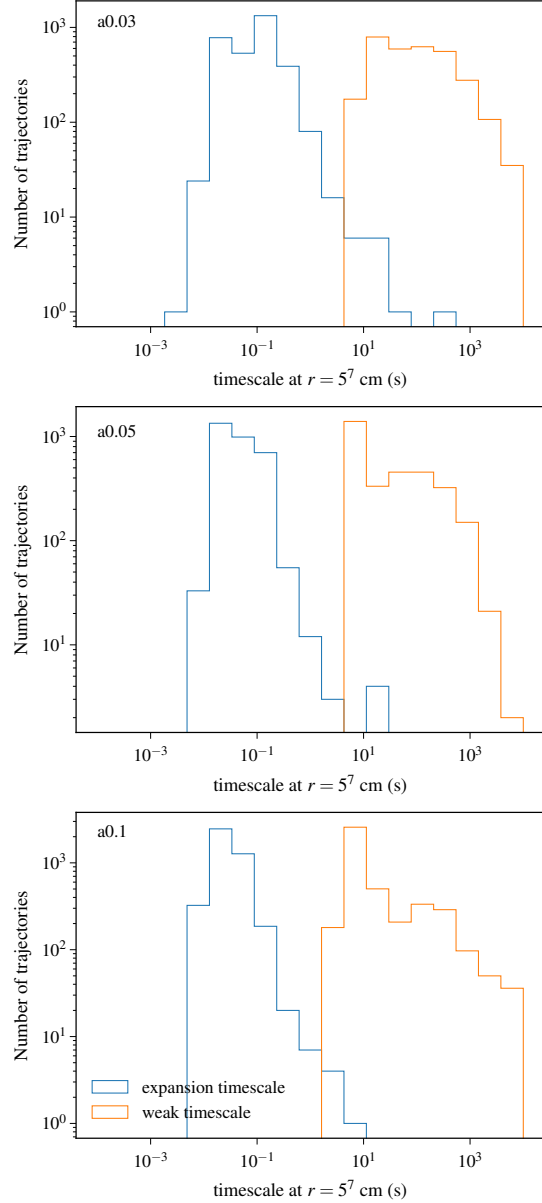


Figure 1. A histogram of the expansion (blue) and weak interaction (orange) timescales at the moment when the tracer particle reaches a radius of 5×10^7 cm for the last time, for the $\alpha 0.03$ (top), base model $\alpha 0.05$ (middle), and $\alpha 0.1$ (bottom) models. The associated log mean is presented in Table 2. There is a decrease in both the expansion and weak interaction timescales for models with an increased viscosity parameter. For the increase between $\alpha 0.03$ and $\alpha 0.05$, these effects cancel out, and Y_e remains approximately unchanged. But, when the viscosity parameter increases to $\alpha = 0.1$, the weak interaction timescale becomes dominant and Y_e increases.

As extensively explained in the midterm report, electron neutrino processes can have a powerful effect on the Y_e . Therefore, the timescale that these processes occur is relevant when examining how the parameters alter Y_e . Four processes must be considered: electron capture with a proton (emitting a neutrino), positron capture with a neutron (emitting an anti-neutrino), neutrino absorption with a neutron, and anti-neutrino absorption with a proton (Just et al. 2021). The rates for each neutrino process are given in the trajectories. The approximate timescale of each process can be calculated by taking the inverse of the rate. The fastest timescale at a given moment is dominant and thus sets the weak interaction timescale, as in Equation 2, where Γ_i is the maximal rate for that time-step.

$$t_{weak} \approx \frac{1}{\Gamma_i} \quad (2)$$

Another relevant timescale is that of the expansion of the disk, which is calculated with Equation 3, where r is the radius, and v_r is the radial velocity (Just et al. 2021).

$$t_{exp} \approx \frac{r}{|v_r|} \quad (3)$$

During the period where the neutrino processes dominate, the absorption processes will increase Y_e , while the emission processes will decrease Y_e . If allowed to continue, Y_e would eventually reach an equilibrium value Y_e^{eq} over the timescale t_{weak} (Just et al. 2021). However, when $t_{weak} > t_{exp}$, Y_e will freeze out and remain constant, preventing Y_e from reaching Y_e^{eq} (Just et al. 2021). Y_e^{eq} can be calculated with Equation 4, where $F_4(-\eta_e)$ and $F_4(\eta_e)$ are the Fermi functions, and η_e is the degeneracy parameter (Janka (2001); Fernández et al. (2019)).

$$Y_e^{eq} = \frac{F_4(-\eta_e)}{F_4(\eta_e) + F_4(-\eta_e)} \quad (4)$$

The Fermi functions can be approximated by Equation 5.

$$F_4(-\eta) = 4! \left(e^{-\eta} - \frac{e^{-2\eta}}{2^5} + \frac{e^{-3\eta}}{3^5} \right) \quad (5)$$

$$F_4(\eta) = F_4(-\eta) + \frac{7\pi^4}{15}\eta + \frac{2\pi^2}{3}\eta^3 + \frac{1}{5}\eta^5$$

The calculation for the degeneracy parameter η_e (eqn. 6) requires the Fermi momentum p_F (eqn. 7) (Bethe et al. (1980); Fernández et al. (2019)).

Model	\bar{t}_{exp} (s)	\bar{t}_{weak} (s)
a0.03	0.087	85.8
base (a0.05)	0.044	31.6
a0.1	0.027	16.9
Lv51	0.047	31.1
base (Lv52)	0.044	31.6
Lv53	0.028	24.5
m2.6	0.047	26.4
base (m2.65)	0.044	31.6
m2.7	0.046	30.4
base (mt0.1)	0.044	31.6
mt0.2	0.053	20.7
mt0.3	0.066	13.0

Table 2. The log mean of the expansion and weak interaction timescales for the time-step when the tracer particle reaches a radius of 5×10^7 cm for the last time. Here the dispersion of the logarithmic mean is a few orders of magnitude from the value. The columns from left to right are model name, log mean of the expansion timescale, and log mean of the weak interaction timescale.

$$\eta_e = \left[\frac{1}{2} \left(\frac{p_F c}{kT} \right)^3 + \sqrt{\frac{1}{4} \left(\frac{p_F c}{kT} \right)^6 + \frac{\pi^6}{27}} \right]^{1/3} + \left[\frac{1}{2} \left(\frac{p_F c}{kT} \right)^3 - \sqrt{\frac{1}{4} \left(\frac{p_F c}{kT} \right)^6 + \frac{\pi^6}{27}} \right]^{1/3} \quad (6)$$

$$p_F = \hbar (3\pi^2 Y_e \frac{\rho}{m_u})^{1/3} \quad (7)$$

Here c is the speed of light, k is the Boltzmann constant, T is the temperature, \hbar is the reduced Planck's constant, ρ is the density, and m_u is the atomic mass unit.

The change in Y_e due to these electron neutrino processes can be calculated by integrating the rate over the time of the simulation, as in Equation 8 (Fernández et al. 2020).

$$\Delta Y_e^i = \int_0^{t_{max}} \Gamma^i dt \quad (8)$$

Then, combine ΔY_e of the neutrino and anti-neutrino, emission and absorption processes to get the total change in electron fraction due to neutrino emission and absorption processes (Equation 9).

$$\Delta Y_e^{em} = \Delta Y_e^{em, \bar{\nu}_e} - \Delta Y_e^{em, \nu_e}$$

$$\Delta Y_e^{abs} = \Delta Y_e^{abs, \nu_e} - \Delta Y_e^{abs, \bar{\nu}_e} \quad (9)$$

The analysis code provides the abundance Y of an element and its associated mass number A . The mass

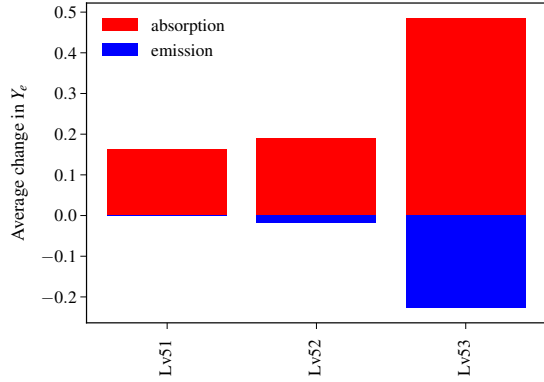


Figure 2. The change in Y_e due to neutrino processes for Lv51, base model (Lv52), and Lv53. The change in Y_e due to absorption is shown in red and the change due to emission is shown in blue. There is an increase in both absorption and emission processes for larger initial neutrino luminosities, exemplified by Lv53, resulting in an increased \bar{Y}_e in Table 3.

fraction Z of each element can be easily calculated with Equation 10, and a range of mass fractions can be summed to attain the mass fraction of that range.

$$Z = Y \cdot A \quad (10)$$

3. RESULTS

The process with the fastest rate, hence shortest timescale, will dominate and have the strongest influence over Y_e . Since each timescale will change during the entire simulation, the relevant comparison is how much each timescale changes during the simulation. Comparing the average expansion timescale and the weak interaction timescale can give insight into how much time passes before freeze-out occurs, which is directly linked to how much neutrino processes affect Y_e . The timescales were calculated using Equations 2 and 3 for the time-step where the tracer particle reaches a radius of 5×10^7 cm for the last time. Then, a histogram of these results was created for each model. Figure 1 shows an example of these plots for the models with varying viscosity parameters. The logarithmic mean, in which the logarithm is taken prior to calculation of the mean, of both timescales was found for each model and presented in Table 2. Here the dispersion of the logarithmic mean of the timescales is a few orders of magnitude from the value.

The change in Y_e due to neutrino processes, ΔY_e , is calculated using Equations 8 and 9. As an example, the results are plotted in Figure 2 for Lv51, base model (Lv52), and Lv53, where ΔY_e^{abs} is in red and ΔY_e^{em} is in blue.

It is also advantageous to plot the entropy as a function of Y_e . Creating this plot is beneficial because it

separates the early neutrino-driven ejecta from the later convective ejecta. Using the data from the trajectories, Figure 3 shows the entropy plots for all models. A color bar was added to indicate when the particle reached the radius 5×10^7 cm for the last time. The early, neutrino-driven ejecta is on the blue end of the color scale, and the later, convective ejecta is on the red end. A value of $t = 0.3$ s was chosen to divide the ejecta populations so that the number of particles in each group could be counted. The fraction of convective (late-time) ejecta particles to total particles are presented in the second column of Table 3.

Model	$\frac{n_{con}}{n_{tot}}$	\bar{Y}_e	$X_{A>130}$
a0.03	0.62	0.26 ± 0.055	0.23
base (a0.05)	0.34	0.26 ± 0.047	0.20
a0.1	0.10	0.28 ± 0.041	0.07
Lv51	0.34	0.25 ± 0.049	0.27
base (Lv52)	0.34	0.26 ± 0.047	0.20
Lv53	0.16	0.35 ± 0.078	0.01
m2.6	0.30	0.25 ± 0.048	0.26
base (m2.65)	0.34	0.26 ± 0.047	0.20
m2.7	0.32	0.27 ± 0.047	0.16
base (mt0.1)	0.34	0.26 ± 0.047	0.20
mt0.2	0.37	0.24 ± 0.054	0.35
mt0.3	0.32	0.23 ± 0.067	0.47

Table 3. The columns from left to right are model name, fraction of convective particles to total particles, mean Y_e and standard deviation, and total mass fraction of elements with $A > 130$.

The mass of each tracer particle can be calculated by taking the torus mass from Table 1 and dividing by 10^4 particles used in the simulation. The mass per particle can be used to create a mass-weighted histogram of Y_e . Figure 4 includes two examples of these plots for the set of models with altered initial neutrino luminosity and central object mass. The mean and standard deviation of the electron fraction for all models is presented in the third column of Table 3.

The results from SkyNet, along with Equation 10, are used to find the mass fraction of each element. The mass fractions are presented in Figure 5 for all models, along with solar abundances for comparison. These mass fractions can be summed over a range of A to obtain the total mass fraction of that range. For the case of r-process elements, the mass fractions for elements with $A > 130$ are summed. The resulting total mass fraction of r-process elements for each model is presented in the fourth column of Table 3.

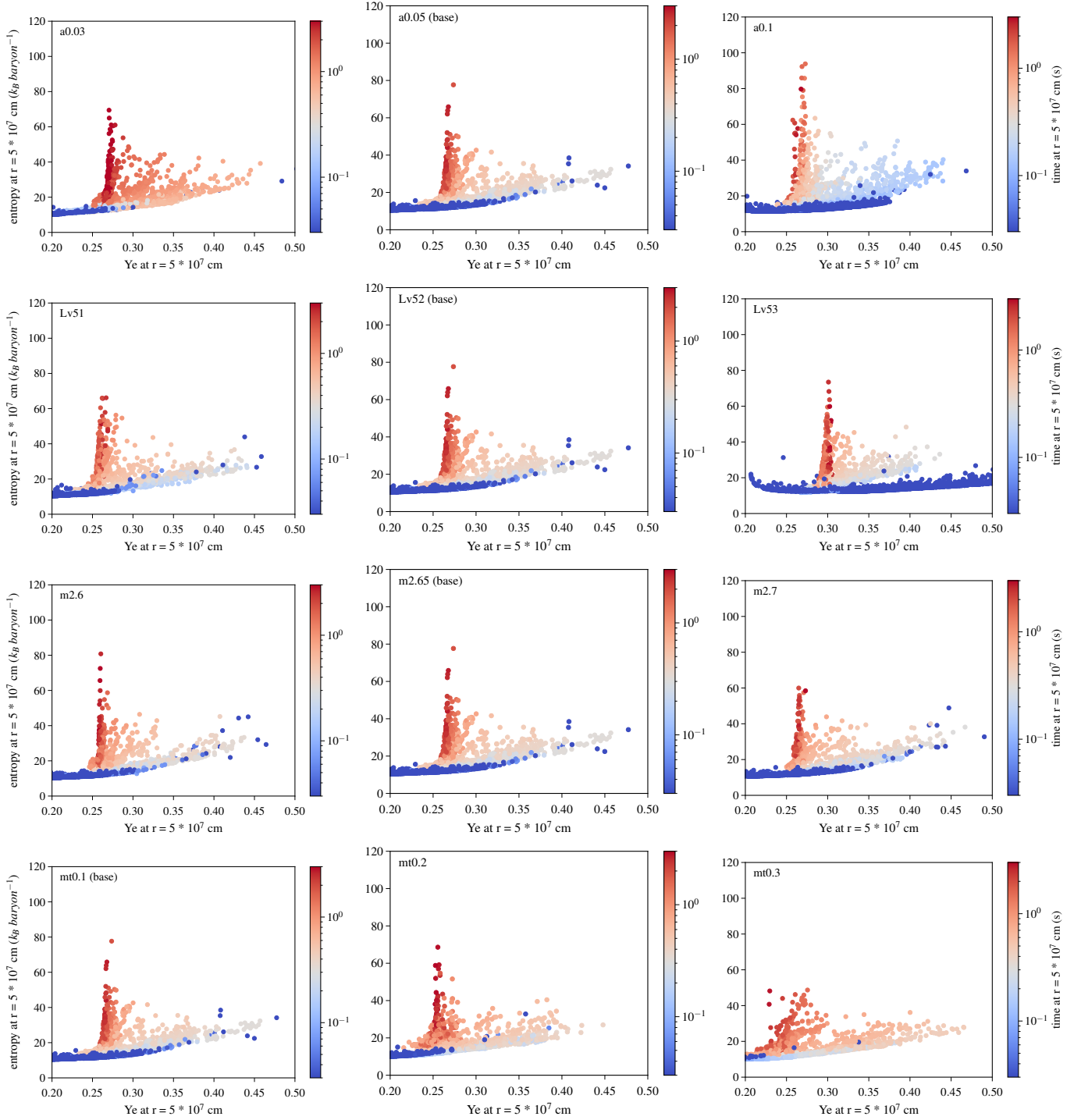


Figure 3. The entropy as a function of Y_e when the tracer particle reaches a radius of $5 \times 10^7 \text{ cm}$ for the last time, for all models. The top row shows models with varying viscosity parameter, the second with varying initial neutrino luminosity, the third with varying central object mass, and the last with varying initial torus mass. A color scale was added to indicate when the particle reaches $r = 5 \times 10^7 \text{ cm}$ for the last time. The early neutrino-driven ejecta is shown in blue, and the later convective ejecta is red. These two populations were roughly separated using $t = 0.3 \text{ s}$ as the boundary. The first and second rows show a shift to higher Y_e for the blue group and few particles in the red group, at a low Y_e , for higher viscosity parameters and higher initial neutrino luminosity, respectively. As opposed to the third row, where there is very little noticeable change in the plots for increased central object mass, the fourth row shows a clear shift toward lower Y_e in the blue population with higher initial torus mass.

4. DISCUSSION

In this section, the results in Section 3 will be put into the context of how the mass fraction of r-process elements changes for different parameters presented in Table 1. Each subsection will focus on a single set of models with one parameter being varied.

4.1. Viscosity Parameter

There are two factors at play when the viscosity parameter is increased. Firstly, increasing viscosity accelerates the evolution of the torus, resulting in a shorter expansion timescale. Hence, Y_e freeze-out will occur earlier, and \bar{Y}_e will be lower. However, this is countered by the second factor, the increased heating in the torus due to the increased viscosity. A hotter torus will have more rapid weak interactions, hence a short weak interaction timescale and a later Y_e freeze-out. Both of these results can be seen in Table 2 and Figure 1, where both \bar{t}_{exp} and \bar{t}_{weak} decrease with an increased viscosity parameter. These two processes will compete to drive Y_e lower or higher. The question is: which process will dominate?

The answer to this question can be found in Table 3. For models a0.03 and a0.05 (base), the viscosity parameter is increased by 0.02. During this increase, the decrease in \bar{t}_{exp} and \bar{t}_{weak} seem to balance each other, as there is no change in the \bar{Y}_e in Table 3. However, the increase from $\alpha = 0.05$ to $\alpha = 0.1$ increases \bar{Y}_e by 0.02, suggesting the weak interaction timescale had a dominant effect on Y_e .

These results are confirmed in the first row of Figure 3, which shows that the early ejecta particles (blue) are shifted to a higher \bar{Y}_e for a higher viscosity parameter. Also, the fraction of particles in the later convective ejecta (red), at the lower Y_e , are much lower for a higher viscosity parameter, which is shown in column 2 of Table 3. Both effects result in a higher average \bar{Y}_e for a0.1.

The increased \bar{Y}_e for a0.1, in the third column of Table 3, is accompanied by an decrease in $X_{A>130}$. As explained in Section 1, this is due to a high neutron density, hence the low electron fraction required for the r-process to occur. In the upper left quadrant of Figure 5, there is a decrease in mass fraction for $A > 130$ when the viscosity parameter is increased. Therefore, it can be confidently said that increasing the viscosity parameter results in fewer heavy elements being produced. It should be pointed out that a minor increase in Y_e resulted in a large decrease in $X_{A>130}$. Again, $Y_e \lesssim 0.25$ is the approximate boundary for the r-process to occur (Metzger 2019). Therefore, a large drop in $X_{A>130}$ for a0.1 is expected.

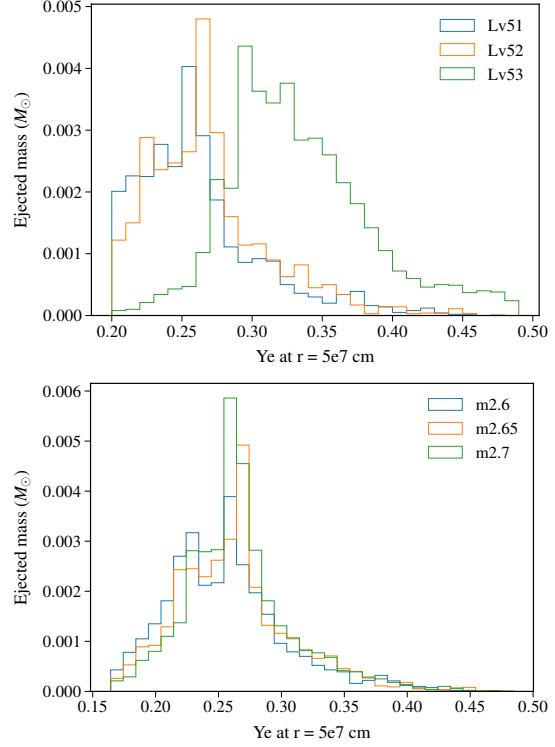


Figure 4. This figure shows the mass-weighted histogram of the electron fraction for the set of models with varying neutrino luminosities (top) and models with varying central object mass (bottom). For these models, a particle mass of $0.1 M_\odot / 10^4$ was used, though this will vary for models with different torus mass. In the top plot, a higher average Y_e is seen for a higher initial neutrino luminosity, resulting in lower $X_{A>130}$. In the bottom plot, there is little variation in Y_e when the central object mass is altered. However, Table 3 shows a slight increase in \bar{Y}_e for a larger central mass, resulting in lower $X_{A>130}$.

4.2. Initial HMNS Neutrino Luminosity

For models Lv51, Lv52 (base model), and Lv53, the initial neutrino luminosity increases by a factor of ten in each subsequent model. Increasing the neutrino luminosity increases the rate of weak interactions and hence decreases the average weak interaction timescale, which can be seen in Table 2. There is no noticeable change in the average weak interaction timescale between models Lv51 and Lv52, but there is a large drop for Lv53. This pattern can also be seen for ΔY_e in Figure 2, where there is a large increase in both emission and absorption processes for Lv53. The result of the increased weak interactions is seen in the second row of Figure 3, where there is a shift of the early, neutrino driven ejecta (blue) towards a higher Y_e for a higher neutrino luminosity. The fraction of particles in the later, convective (red) group, with lower Y_e , is also much lower for Lv53; see Table 3. The conclusion that can be drawn is that there

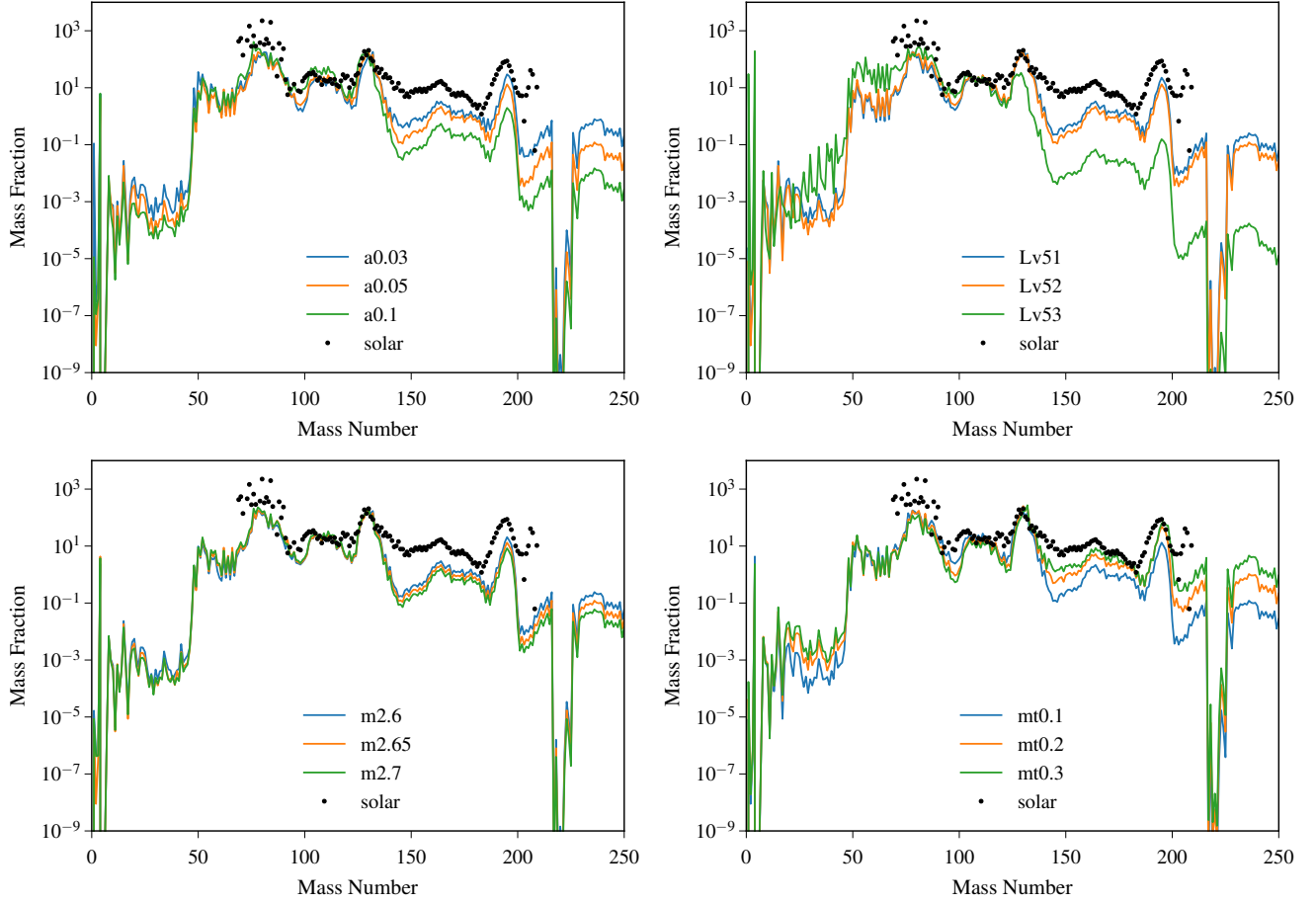


Figure 5. The mass fraction of all elements up to $A = 250$ for all models. The upper left plot shows models with varying viscosity parameter, the upper right with varying initial neutrino luminosity, the lower left with varying central object mass, and the lower right with varying initial torus mass. The solar abundances, scaled to match the second r-process peak, are also included for comparison. In the upper left quadrant, fewer heavy elements are produced for models with an increased viscosity parameter. In the upper right quadrant, an increase in initial neutrino luminosity results in fewer heavy elements being produced. In the lower left quadrant, there is a minimal increase in \bar{Y}_e in Table 3, resulting in a slightly lower mass fraction of heavy elements ($A > 130$) when the central object mass is increased. The lower right quadrant shows an increase in the mass fraction of heavy elements produced for larger initial torus mass.

should be a higher \bar{Y}_e for Lv53 as compared to Lv51 and Lv52. Table 3 and Figure 4 (top) clearly agrees with this prediction. As expected, Lv53 produces a much lower $X_{A>130}$ due to the increased Y_e . This outcome is also confirmed by Figure 5, which shows fewer heavy elements for higher neutrino luminosities.

4.3. Central Object Mass

The variation in Y_e for models where the central mass is altered are more difficult to explain, since there is no clear pattern in the expansion timescale, weak interaction timescale, the change in Y_e due to neutrinos, and in the third row of Figure 3. When looking at Figure 4 (bottom) there appears to be no variation in Y_e , but the \bar{Y}_e in Table 3 shows a minor increase in Y_e for a larger central mass. Although this increase is minor, the out-

come of a minor change has a larger effect on $X_{A>130}$. The explanation requires some discussion on the physical consequences of increasing the central mass.

The conservation of energy equation for a particle, at radius R and with mass m , in the torus orbiting around a central object of mass M is

$$\frac{GMm}{R} = kT \quad (11)$$

where T is the temperature of the particle, G is the gravitational constant, and k is the Boltzmann constant. Since everything is constant except T and M , it can be said that $M \propto T$. Using Equations 4 and 5, it can be found that Y_e^{eq} is roughly proportionality is $Y_e^{eq} \propto \frac{1}{\eta}$. Equation 6 shows that $\eta \propto \frac{1}{T}$. Therefore, $Y_e^{eq} \propto T \propto M$. So, when the mass of the central object is increased,

the equilibrium of Y_e is also increased. This drives \bar{Y}_e upward and results in a lower $X_{A>130}$, as shown in Table 3 and Figure 5.

4.4. Initial Torus Mass

For the final category of models, those with altered initial torus mass, there is a clear pattern for \bar{t}_{exp} and \bar{t}_{weak} in Table 2. For increasing torus mass, there is an increase in \bar{t}_{exp} and a decrease in \bar{t}_{weak} . Both effects promote the dominance of the weak interaction timescale and thus drive Y_e to a lower value, as shown in Table 3. This conclusion is confirmed by the results in the third row of Figure 3, where the average Y_e of the blue population is shifted to a lower Y_e for a larger initial torus mass.

The physical reason for this outcome lies in the properties of the torus. The torus' radius, and hence volume, remains the same in all models. So, when the initial torus mass increases, the density and temperature also increase. An increase in temperature also increases the rate of weak interactions, decreasing t_{weak} and driving Y_e to lower values. Therefore, there is a decrease in \bar{Y}_e and an increase in $X_{A>130}$ for larger initial torus mass, as seen in Table 3 and Figure 5.

5. CONCLUSION

For this project, I worked with the results of several hydrodynamic simulations of HMNS disk outflows,

which were published in Fahlman & Fernández (2018). The parameters of these models were chosen to resemble those of the gravitational wave detection GW170817. I performed further analysis on this data by post-processing them with SkyNet, a nuclear reaction network code that simulates nucleosynthesis in the ejecta of a HMNS torus. I examined how varying the parameters of the models can affect the mass fraction of heavy elements (specifically r-process elements) produced. One of the most important factors was how the parameters changed the electron fraction, as a low electron fraction is required for the r-process to occur. The main results are summarized in the third and fourth columns of Table 3. The general conclusions that can be made are that a low viscosity parameter, low initial neutrino luminosity, low central HMNS mass, and a high initial torus mass promoted an increase of heavy elements being produced.

The known parameters of NS-NS mergers have large uncertainties. Therefore, it is valuable to do studies, such as this one, with many models that have slightly different parameters so the affect of varying parameters can be closely examined. GW170817 provided evidence that NS-NS mergers are a significant source of r-process elements. Table 3 agrees with this prediction, in that large amounts of r-process elements are produced when the HMNS has certain select parameters.

REFERENCES

- Bethe, H. A., Applegate, J. H., & Brown, G. E. 1980, *The Astronomical Journal*, 241, 343. <https://ui.adsabs.harvard.edu/abs/1980ApJ...241..343B/abstract>
- Burbidge, E. M., Burbidge, G. R., Fowler, W. A., & Hoyle, F. 1957, *Reviews of Modern Physics*, 29, doi: 10.1103/RevModPhys.29.547
- Cameron, A. G. W. 1957, *Publications of the Astronomical Society of the Pacific*, 69, 201, doi: 10.1086/127051
- Curtis, S., Mösta, P., Wu, Z., et al. 2021, *Monthly Notices of the Royal Astronomical Society*, 1. <https://arxiv.org/abs/2112.00772>
- Fahlman, S., & Fernández, R. 2018, *The Astrophysical Journal Letters*, 869, doi: 10.3847/2041-8213/aaf1ab
- Fernández, R., Foucart, F., & Lippuner, J. 2020, *Monthly Notices of the Royal Astronomical Society*, 497, 3221, doi: 10.1093/mnras/staa2209
- Fernández, R., Tchekhovskoy, A., Quataert, E., Foucart, F., & Kasen, D. 2019, *Monthly Notices of the Royal Astronomical Society*, 482, 3373. <https://arxiv.org/abs/1808.00461v2>
- Janka, H.-T. 2001, *Astronomy and Astrophysics*, 368, 527, doi: 10.1051/0004-6361:20010012
- Just, O., Goriely, S., Janka, H.-T., Nagataki, S., & Bauswein, A. 2021, *Monthly Notices of the Royal Astronomical Society*, 509, 1377, doi: 10.1093/mnras/stab2861
- Kasen, D., Metzger, B., Barnes, J., Quataert, E., & Ramirez-Ruiz, E. 2017, *Nature*, 551, 80, doi: 10.1038/NATURE24453
- Metzger, B. D. 2019, *Annals of Physics*, 410, doi: 10.1016/j.aop.2019.167923
- Siegel, D. M. 2019, *The European Physical Journal A*, 55, doi: 10.1140/epja/i2019-12888-9